Granular texture

Farhang Radjai*, Emilien Azéma*, Jack Lanier**

* *Laboratoire de Mécanique et Génie Civil, Université Montpellier 2, CNRS, Place Eugène Bataillon, 34095 Montpellier cedex 05, France.*
** *Laboratoire Sols Solides Structures Risques, Domaine Universitaire, BP53, 38041 Grenoble Cedex 9, France.*

1 Introduction

Granular materials consist of densely packed solid particles and a pore-filling material which can be a fluid or a solid matrix. The particles interact via elastic repulsion, friction, adhesion and other surface forces. By nature, the length scales involved in these contact interactions are well below the particle size. External loading leads to particle deformations as well as cooperative particle rearrangements. The particle deformations are of particular importance in powder metallurgy, for example, but the particles may be considered as quasi-rigid beyond the elastic response times.

The contact network and pore space are the two facets of the microstructure of granular materials, to which we will refer as *granular texture*. At the particle scale, the granular texture involves three basic vectors from which other local geometrical variables can be defined: 1) the *branch vector* $\vec{\ell} \equiv \ell\vec{n}'$ joining the centers of contacting particles, 2) the contact orientation vector (contact normal) $\vec{n}$ defined as the unit vector normal to the particle boundary at the contact zone α and 3) the *contact vectors* $\vec{c}$ joining the particle centers to the contact point; see Fig. 1. The reaction forces $\vec{f}$ and $-\vec{f}$ acting on two particles at their contact zone have a unique application point which may be considered as their contact point in the case of extended contacts such a face-face contact between two polyhedral particles.

Two different local frames can be associated with a pair of contacting particles: 1) The frame defined by the contact normal $\vec{n}$ and two orthogonal unit vectors $(\vec{t}, \vec{s})$ in the contact plane (tangent to the two particles at the contact point); 2) The frame defined by the "radial" unit vector $\vec{n}'$ and two orthogonal unit vectors $(\vec{t}', \vec{s}')$ in a orthoradial plane (orthogonal to the branch vector). These

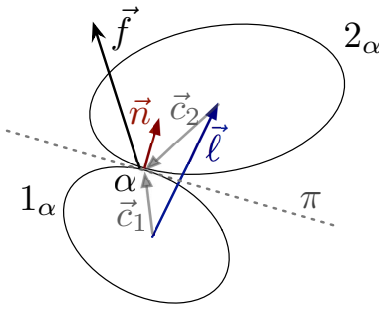

Fig. 1. Local vectors at the contact α between two particles 1_α and 2_α: branch vector $\vec{\ell}$, contact normal $\vec{n}$, contact force $\vec{f}$ and contact vectors $\vec{c}$.

two frames coincide in the case of spherical particles. In 2D, the local frame is uniquely defined by a single tangent unit vector t or t'.

The granular texture is disordered with many different variants depending on the *composition* (particles shapes and sizes), interactions and assembling procedure. The granular disorder is essentially characterized by the fact that, as a result of geometrical exclusions among particles, the local vectors vary discontinuously from one contact to another. In other words, the local environments fluctuate in space. The contact network evolves with loading so that the local environments fluctuate also in time. The highly inhomogeneous distribution of contact forces reflects granular disorder in static equilibrium. In particular, the *force chains* reveal long-range correlations whereas the presence of a broad population of very weak forces results from the *arching effect*. The force and fabric anisotropies are two complementary aspects of stress transmission, and they can be employed in local (particle-scale) description of granular media in the quasi-static state.

The geometrical changes of granular texture are at the origin of the complex rheology of granular materials. These changes are highly nonlinear, involving creation and loss of contacts, rotation frustration and frictional sliding. They depend on the dissipative nature of contact interactions and steric exclusions among particles. In quasi-static deformation, various features of the plastic behavior such as shear strength and dilatancy can be traced back to the evolution of granular texture.

We introduce below several concepts and tools for the description of granular texture and kinematics with examples and illustrations from discrete element simulations (molecular dynamics and contact dynamics). We first consider the description of granular texture in terms of particle positions and contact orientations. Then, the kinematics and mechanisms of plastic deformation are analyzed.

2 Description of granular texture

The granular texture is generally described in terms of the distributions of the vectors $\vec{n}$, $\vec{\ell}$ and $\vec{c}$ associated with the local geometry. At the lowest order, the relevant scalar parameters concern the *connectivity* of this network. At higher orders, the anisotropy of the texture is described by *fabric tensors*. Such definitions rely either directly on the local vectors or on a partition of the space occupied by the particles in terms of Voronoi cells or Delaunay tessellation.

2.1 Particle connectivity

The connectivity of a granular assembly refers to the set of force-bearing (active) contacts. A number of contacts do not participate in force transmission. These "inactive" contacts and "floating" particles (with no active contact) are generally removed from the statistics. The connectivity is described at the lowest order by the *coordination number* defined as the average number z of contact neighbors per particle. This is a crude scalar information as compared to the complex arrangement of the particles, but it is well known that the compactness of the texture controls the stress-strain behavior under monotonic shearing. Remark that for particles of arbitrary shape (polygones, polyhedra, ...), different types of contact (edge-to-edge, face-to-face, etc) exist, and they can be distinguished by defining a distinct coordination number for each type of contact.

Fig. 3 shows the evolution of z for two different packings during a biaxial compression test performed by means of the contact dynamics method as a function of the cumulative shear strain $\varepsilon_q = \varepsilon_1 - \varepsilon_2$ in 2D. The first sample, denoted S1, is composed of 14400 regular pentagons of three different diameters: 50% of diameter 2.5 cm, 34% of diameter 3.75 cm and 16% of diameter 5 cm. The second sample, denoted S2, is composed of 10000 discs with the same particle size distribution. Both samples were prepared by isotropic compaction with zero friction. Hence, at the initial state, both numerical samples are in an isotropic stress state. The solid fraction is $\rho_0 = 0.80$ for S1 and $\rho_0 = 0.82$ for S2. Figure 2 displays snapshots of the two packings at the beginning of biaxial compression. The coefficient of friction during compression is 0.4 between the particles and 0 between the walls and the particles. The coordination number evolves towards a steady-state value in both samples with a higher value for S2 ($\simeq 3.85$) than for S1 ($\simeq 3.75$). The difference is, however, much less important than in the initial configuration ($\simeq 3.95$ for S2 compared to $\simeq 3.20$ for S1) prepared by means of isotropic compaction (Azma et al. [2007]).

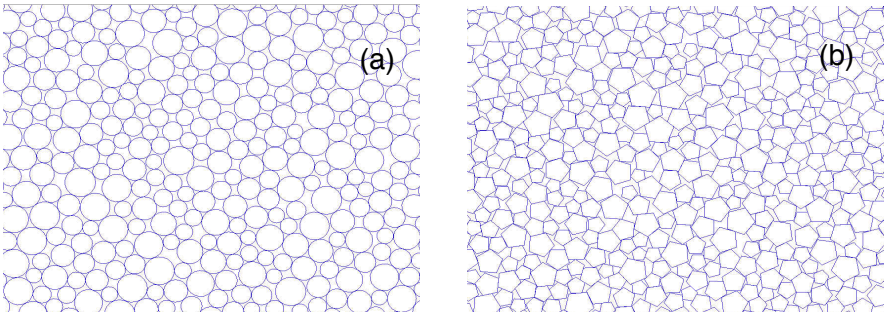

Fig. 2. Snapshots of a portion of the samples S2 (a) and S1 (b) composed of circular and pentagonal particles, respectively.

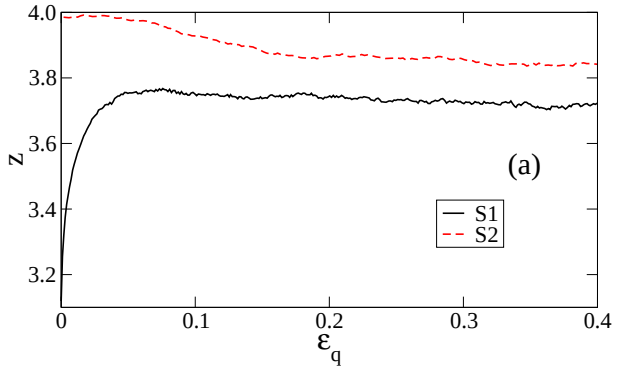

Fig. 3. Coordination number z as a function of cumulative shear strain ε_q for two samples S1 and S2 during a biaxial compression test simulated by the contact dynamics method.

The connectivity of the contact network can be characterized in more detail by the proportion $P(c)$ of particles with exactly c contact neighbors. The coordination number is the mean value of c : $z = \sum_c cP(c)$. The connectivity $P(c)$ of the particles is plotted in Fig. 4 for S1 and S2 at $\varepsilon_q = 0.3$. The two plots are nearly identical with a peak at $c = 4$. In both samples, the fraction of particles with 5 contacts is higher than that with 3 contacts. This shows that the connectivity does not reflect the difference in texture between the two packings although a qualitative difference exists in terms of the fabric and force anisotropies (see below).

2.2 Contact network anisotropy: fabric tensors

The shear strength of dry granular materials is generally attributed to the buildup of an anisotropic texture during shear due to friction between the particles and as a result of steric effects depending on particle shapes and sizes (Oda et al. [1980], Cambou [1993], Radjai et al. [2004]). Several methods have been used to quantify the fabric (structural) anisotropy of granular materials (Satake [1982], Rothenburg and Bathurst [1989], Oda and Iwashita [1999],

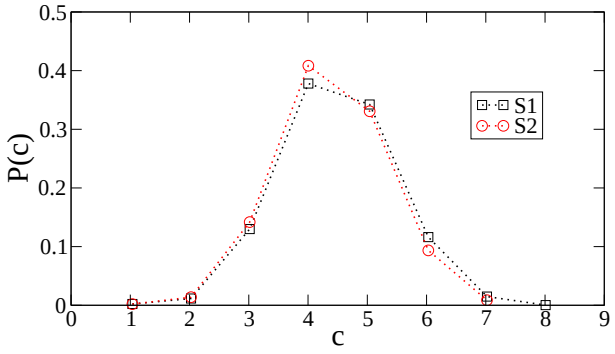

Fig. 4. Connectivity diagram for the samples S1 and S2 expressing the fraction $P(c)$ of particles with exactly c contacts in the steady state.

Kanatani [1984]).

2.2.1 General case

Following Kanatani, let us consider a physical quantity carried by a set of unit vectors (Kanatani [1984]). These vectors may be contact normals $\{\vec{n}\}$ or branch unit vectors $\vec{n}'$ (unit vector along the branch vector) inside a granular sample. Let us assume that N measurements are obtained from this sample: $\{\vec{n}^{(1)}, \cdots \vec{n}^{(N)}$. From these experimental values, we define an experimental probability density function $P_{exp}(\vec{n})$ which can be approximated by a theoretical distribution $P(\vec{n})$. Since the vectors $\vec{n}^i$ are unit vectors, P_{exp} and P are defined on a unit sphere in 3D or a unit circle in 2D, denoted by $\mathcal{S}$ in the following. By definition, we have $P(\vec{n}) \geq 0$ and $\int_{\mathcal{S}} P(\vec{n}) d\Omega = 1$. Remark also that the contact orientations have no intrinsic parity, so that $P(\vec{n}) = P(-\vec{n})$.

The "best" theoretical approximation may be obtained by means of the least square method which amounts to minimizing the function

$$E = \int_{\mathcal{S}} \{P(\vec{n}) - P_{exp}(\vec{n})\}^2 d\Omega \tag{1}$$

with respect to the parameters involved in the definition of $P(\vec{n})$. Let P be expanded as a polynomial sum

$$P(\vec{n}) = C_0 + C_{ij} n_i n_j + C_{ijkl} n_i n_j n_k n_l + \text{h.o.t.} \tag{2}$$

where odd terms have been dropped due to the even parity of P. In this form, the function P is parametrized by the tensors $C_{ij\ldots}$ of increasing order. It can be shown that for an approximation of order m, all terms of order below m should be omitted since they can be expressed through the higher-order terms. For example, using the identity tensor I, we can write $C_{ij} n_i n_j = (C_{ij} I_{kl}) n_i n_j n_k n_l$,

since $I_{kl}n_k n_l = 1$. Hence, the most general polynomial expression of order m is simply given by

$$P(\vec{n}) = C_{i_1 i_2 \ldots i_m} n_{i_1} n_{i_2} \ldots n_{i_m} \tag{3}$$

for $i_k = 1, 2, 3$ in 3D and $i_k = 1, 2$ in 2D. The minimization of E defined by equation [1] with the expression of P given by [3] leads to a linear set of equations

$$A_{\alpha\beta} C_\beta = F_\alpha \tag{4}$$

where α and β design the collective indices $j_1 j_2 \ldots j_m$ and $i_1 i_2 \ldots i_m$, respectively, with

$$A_{\alpha\beta} = \int_{\mathcal{S}} n_{i_1} n_{i_2} \ldots n_{i_m} \; n_{j_1} n_{j_2} \ldots n_{j_m} d\Omega \tag{5}$$

and

$$F_\alpha = \int_{\mathcal{S}} P_{exp}(\vec{n}) n_{j_1} n_{j_2} \ldots n_{j_m} d\Omega \tag{6}$$

The tensor F_α is a symmetric tensor of order m that represents the mean value of the product $n_{j_1} n_{j_2} \ldots n_{j_m}$:

$$F_{i_1 i_2 \ldots i_m} = \langle n_{i_1} n_{i_2} \ldots n_{i_m} \rangle = \frac{1}{N} \sum_{k=1}^{N} n_{i_1}^k n_{i_2}^k \ldots n_{i_m}^k \tag{7}$$

This tensor is often called *fabric tensor* of order m. It is symmetric and involves $(m+1)(m+2)/2$ and $m+1$ independent elements in 3D and 2D, respectively. The fabric tensors contain all the relevant directional information of the considered quantity in the space of contact orientations. However, the intuitive meaning of these tensors is not straightforward to grasp (Kanatani [1984]).

An equivalent description of directional data is given by considering the following expansion in terms of deviatoric tensors $D = C - I$:

$$P(\vec{n}) = \frac{1}{\Omega} \{1 + D_{ij} n_i n_j + D_{ijkl} n_i n_j n_k n_l + \text{h.o.t.}\} \tag{8}$$

These tensors are fully symmetric, i.e. $D_{..i..j..} = D_{..j..i..}$, and $tr(D) = 1$.

2.2.2 Case of 2D data

For 2D data, the above tensors are defined by two independent elements, and the expansion given in (8) is equivalent to a Fourier expansion

$$P(\vec{n}) = \frac{1}{2\pi}\{1 + a_2\cos 2\theta + b_2 \sin 2\theta + \cdots \\ + a_{2m}\cos 2m\theta + b_{2m}\sin 2m\theta + h.o.t.\} \tag{9}$$

where θ is the orientation of $\vec{n}(\cos\theta, \sin\theta)$. The coefficients a_i and b_i represent the anisotropy of the texture at different orders. If the Fourier expansion is truncated beyond the second term, we have

$$P(\vec{n}) = C_{ij}n_i n_j = \frac{1}{2\pi}\{1 + D_{ij}n_i n_j\} \tag{10}$$

with $C_{ij} = 4\langle n_i n_j\rangle - I_{ij}$ and $D_{ij} = C_{ij} - I_{ij}$. If θ_c is the orientation of the major principal direction of D and a_c the difference between its principal values, the second-order expansion of P can be written as

$$P(\vec{n}) = \frac{1}{2\pi}\{1 + a\cos 2(\theta - \theta_c)\} \tag{11}$$

In this expression, a is the second-order fabric anisotropy. The above expression provides a reasonable approximation for a unimodal distribution of the data. Otherwise, higher-order anisotropies should be taken into account.

Equation 11 is related to the second-order fabric tensor by

$$F_{\alpha\beta} = \frac{1}{\pi}\int_0^\pi n_\alpha(\theta)n_\beta(\theta)P(\theta)d\theta \equiv \frac{1}{N_c}\sum_{c\in V} n_\alpha^c n_\beta^c, \tag{12}$$

where α and β design the components in a reference frame, and N_c is the total number of contacts in the control volume V. By definition, $tr(F) = 1$. The anisotropy of the contact network is given by the difference between the principal values F_1 and F_2 of F. It is easily shown that

$$a = 2(F_1 - F_2). \tag{13}$$

For fixed coordinates, with the x-axis pointing along a direction θ', we can also define a "signed anisotropy" a' by

$$a' = 2(F_1 - F_2)\cos 2(\theta_c - \theta'), \tag{14}$$

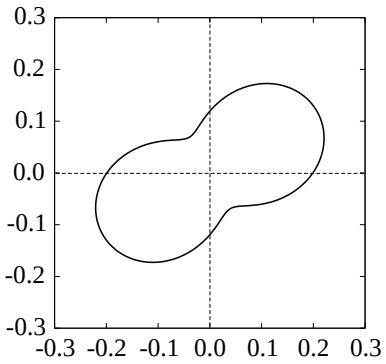

Fig. 5. Second-order approximation of the probability density $P(\theta)$ plotted in polar coordinates for $a = 0.5$ and $\theta_c = \pi/6$.

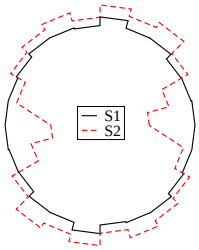

Fig. 6. Polar representation of the probability density function $P(\theta)$ of contact normal directions θ for the samples S1 and S2 in the steady state.

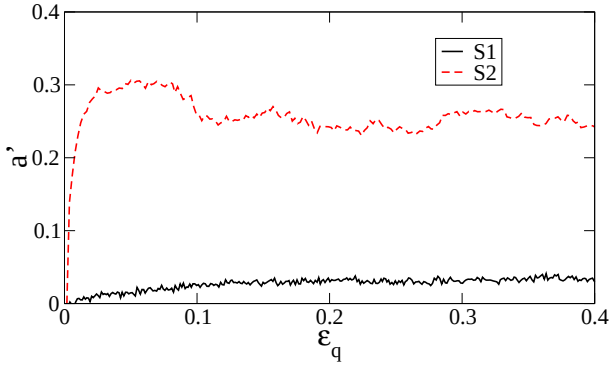

Fig. 7. Evolution of the "signed" anisotropy a' with cumulative shear strain ε_q for the samples S1 and S2.

where θ_c is the major principal direction of the fabric tensor. For $\theta' = \theta_c$, we have $a' = a$. In polar coordinates, equation (11) has a "peanut" shape for $0 \leq a_c \leq 1$. It is reduced to a circle in the limit of an isotropic set for which $a_c = 0$; see Fig. 5.

Figure 6 displays a polar representation of $P(\theta)$ for the samples S1 and S2 at $\varepsilon_q = 0.3$ (Azma et al. [2007]). We observe a nearly isotropic distribution for the pentagon packing in spite of shearing whereas the disk packing is markedly anisotropic. The distribution is clearly unimodal and a (second-order) Fourier expansion provides a good approximation.

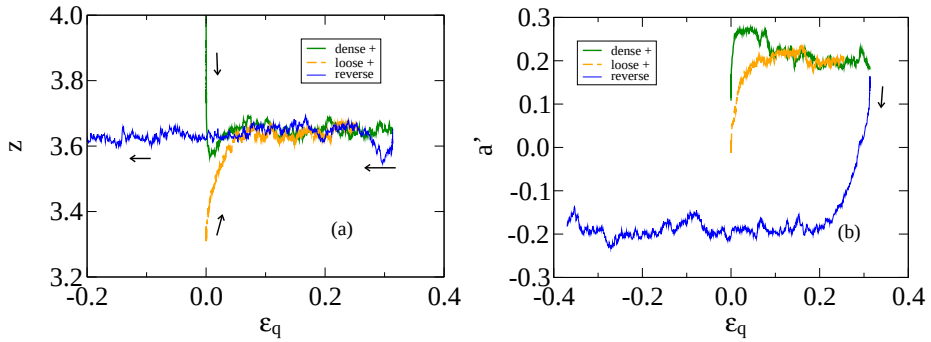

Fig. 8. Evolution of the coordination number z and "signed" anisotropy a' with cumulative shear strain ε_q for a loose sample and a dense sample in simple shear and in reversed simple shear from the steady state.

The evolution of a' is shown in Fig. 7 as a function of ε_q for S1 and S2. The privileged direction of the contacts θ_c is vertical in both packings. In both cases, a' increases from 0 (as a result of the initial isotropic compression) and tends to a steady value at large strains. The low anisotropy of the pentagon packing results from a particular organization of the force network in correlation with the orientations of side-to-side and vertex-to-side contacts in the packing.

The evolution of z and a' is shown in Fig. 8 for simple shear starting from a loose sample, starting from a dense sample and during a reversed simple shear from the steady state, for a 2D system of disks (Radjai and Roux [2004]). We see that both z and a evolve during the transients (at the beginning of shear where the material is in an isotropic state and in the transient following shear reversal). Interestingly, shear reversal causes initially z to decrease before the steady state is reached again in the opposite direction with the steady-state value of z.

2.2.3 Case of 3D data

The probability density $P(\vec{n})$ of unit vectors $\vec{n}$ can be expanded according to equation 10. This expansion in 3D at leading order is equivalent to a representation of the data in terms of spherical harmonics (Ouadfel and Rothenburg [2001], Azéma et al. [2008]). Let $\mathcal{A}(\vec{n}')$ be the set of branch vectors pointing in the direction $\vec{n}' \equiv (\theta, \phi)$ up to a solid angle $d\Omega$, and $N_c(\vec{n}')$ its cardinal. The angles θ and ϕ are shown in Fig. 9. By definition, we have

$$P(\vec{n}') = \frac{N_c(\vec{n}')}{N_c} \tag{15}$$

We consider here axisymmetric (symmetry by revolution) conditions as in a classical triaxial test. Then, the function $P(\vec{n}')$ is independent of ϕ. There are

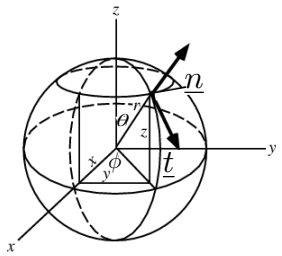

Fig. 9. Spherical coordinates.

nine second-order basis functions $Y_m^l(\theta, \phi)$. But only the functions compatible with the symmetries of the problem, namely independent with respect to ϕ and π-periodic as a function of θ, are admissible under axisymmetric conditions. Hence, the only admissible functions are $Y_0^0 = 1$ and $Y_2^0 = 3\cos^2\theta - 1$, and we have

$$P(\vec{n}') = \frac{1}{4\pi}\{\ 1 + a\ [3\cos^2(\theta - \theta_b) - 1]\ \} \tag{16}$$

where a is the anisotropy of branch vector orientations and θ_b their privileged orientation. The function $P(\vec{n}')$ is normalized to 1 ($\int_{\mathcal{S}} P(\vec{n}')d\Omega = 1$). We will refer to this expansion at leading order in spherical harmonics as the *harmonic approximation*.

Figure 11 shows a polar representation of $P(\vec{n}')$ for two samples of polyhedra (S'1) and spheres (S'2) subjected to triaxial compression by means of contact dynamics simulations. The two samples are displayed in Fig. 10. The first sample (S'1) is composed of 36933 polyhedra of irregular shape involving at least 12 faces and 8 vertices and at most 70 faces and 37 vertices. The second sample (S'2) is composed of 19998 spheres with exactly the same size distribution as in S'1. During triaxial compression, the coefficient of friction is 0.5 between the particles and 0 with the walls. The harmonic approximation is well fit to the distribution $P(\vec{n}')$ for both sheared samples. It is remarkable that the anisotropy is lower for polyhedra compared to spheres.

2.3 Branch vectors

In the last section, we considered the fabric tensors constructed from the branch vectors $\vec{\ell} \equiv \ell\vec{n}'$. The branch vector lengths ℓ can be characterized by their probability density function $P_l(\vec{n}')$ and their angular average function $\langle\ell\rangle(\vec{n}')$ defined by

$$\langle\ell\rangle(\vec{n}') = \frac{1}{N_c(\vec{n}')} \sum_{c\in\mathcal{A}(\vec{n}')} \ell^c \tag{17}$$

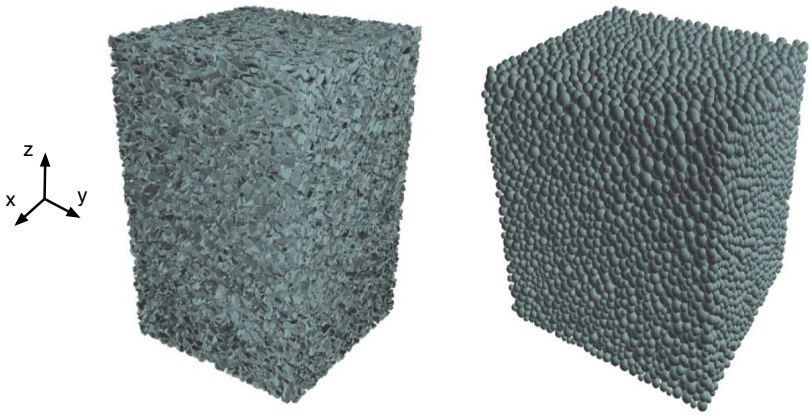

Fig. 10. Snapshots of the two packings S'1 (polyhedra) and S'2 (spheres) simulated by the contact dynamics method. The walls are not shown.

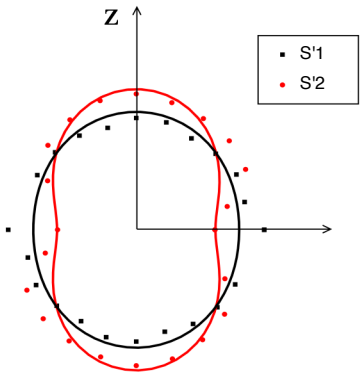

Fig. 11. Polar representation of the density probability $P(\vec{n}')$ for S'1 et S'2 at the sheared state. The solid lines are harmonic fits to the data points.

where $\mathcal{A}(\vec{n}')$ is the set of branch vectors pointing in the direction $\vec{n}' \equiv (\theta, \phi)$ up to a solid angle $d\Omega$ and $N_c(\vec{n}')$ is its cardinal.

One example is shown in Fig. 12 for triaxially sheared samples of polyhedra and spheres as a function of the zenith angle θ of the branch unit vectors $\vec{n}'$ (Azéma et al. [2008]). The data points are fitted by a harmonic expansion:

$$\langle \ell \rangle(\vec{n}') = \ell_m \{ \, 1 + a_l \, [3\cos^2(\theta - \theta_l) - 1] \, \} \tag{18}$$

where ℓ_m is the mean branch vector length, a_l is the branch vector length anisotropy and θ_l is the angle at which the largest distance between particle centers occurs.

The value of a_l is generally weak. But it can become more important for elongated or highly polydisperse particles. In Fig. 12, its value is about 0.1 for polyhedral particles generated from spheres. An interesting behavior recently evidenced by numerical simulations is that the fabric anisotropy a for branch

vector orientations of polydisperse packings of circular particles decreases as the size span becomes broader while the branch vector length anisotropy a_l increases at the same time. The polydispersity is characterized by the size span $s = (d_{max} - d_{min})/(d_{max} - d_{min})$, where d_{min} and d_{max} are the extreme particle diameters. Fig. 13 shows the evolution of a and a_l, as well as the normal and tangential force anisotropies a'_n and a'_t that will be discussed below, as a function of s (Voivret [2008]).

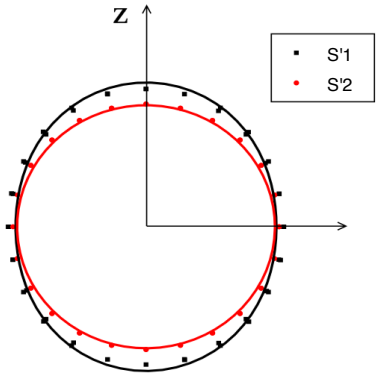

Fig. 12. Polar representation of the average branch vector length $\langle \ell \rangle(\theta)$ for the triaxially compressed samples S'1 and S'2 as a function of the zenith angle θ.

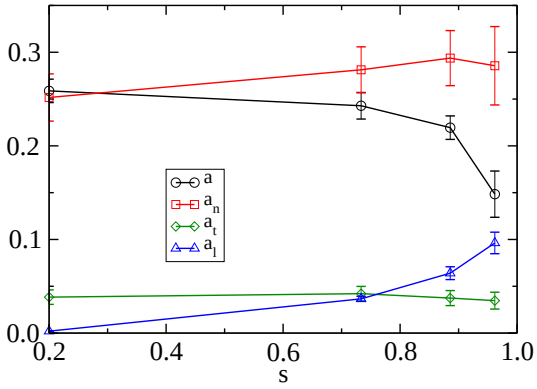

Fig. 13. Evolution of fabric and force anisotropies a, a_l, a'_n and a'_t as a function of the size span s in sheared packings of 10^4 circular particles simulated by the contact dynamics method.

2.4 Evolution of granular texture

The granular texture evolves mainly due to contact loss and gain. The fraction of lost and gained contacts depends on the contact orientation. The maximum contact gain occurs along the major principal strain rate direction (compression axis) whereas the maximum contact loss occurs along the minor strain rate direction (direction of extension). The number of contacts is stationary

at intermediate directions where the number of lost contacts equals to the number of gained contacts.

The evolution of the distribution $N(\theta)$ of contact orientations can be represented as a function $S(\theta)$ defined by

$$S(\theta) = \frac{N_f(\theta)}{N_i(\theta)} = 1 + \frac{\Delta N(\theta)}{N_i\theta)} \tag{19}$$

where N_i and N_f are the initial and final distributions. When for a direction θ there is more gain than loss, we have $S(\theta) > 1$. In the opposite case, i.e. when contact loss is dominant, $S(\theta) < 1$. The fact that harmonic approximation fits generally well $S(\theta)$ suggests that a second-order tensor A can be used to model the texture evolution so that

$$S(\theta) = A\vec{n} \cdot \vec{n} = n_i A_{ij} n_j \tag{20}$$

where $\vec{n}$ here designs a unit vector with orientation θ. In the case of biaxial compression, the principal directions of A are imposed by the boundary conditions so that the stress and incremental strain principal directions coincide. In order to check the validity of this tensorial representation, we consider a test implying the rotation of the principal directions of the incremental strain tensor. Then, the principal directions of stress σ, strain ε and incremental strain $\Delta\varepsilon$ are coincident. Experimental data suggest that A and $\Delta\varepsilon$ are generally coaxial. Hence, the tensor A may be expressed as a function of $\Delta\varepsilon$ as

$$A_{\alpha\beta} = a\delta_{\alpha\beta} + b\Delta\varepsilon_{\alpha\beta} \tag{21}$$

where a and b are functions of incremental strain invariants. Experimental tests indicate that a is close to 1, so that the evolution of texture may be represented by

$$\frac{\Delta N}{N}(\theta) = b\ n_\alpha\ \Delta\varepsilon_{\alpha\beta}\ n_\beta = b\ \Delta\varepsilon_n(\theta) \tag{22}$$

where $\Delta\varepsilon_n(\theta)$ is the increment of elongational deformation in the direction θ. Equation [22] allows one to evaluate the evolution of the texture from the incremental macroscopic deformation. This equation predicts that the number of contacts is constant ($\Delta N(\theta) = 0$) along the zero extension lines $\Delta\varepsilon_n(\theta) = 0$.

2.5 Space partition: tessellation

A useful geometrical representation of granular texture consists of dividing the space occupied by the particles into contiguous cells. This procedure is called "tessellation" and it can be considered as a first step towards a continuum description of the material. The most common tessellation rules are presented in this section.

2.5.1 Voronoi cells

Let us consider a set of material points M_k with $k \in [1, N]$. These points may be the particle centers. The Voronoi cell (C_n) attributed to the point M_n is the polygonal domain defined by the nearest points P of M_n:

$$P \in (C_n) \quad \text{if} \quad PM_n < PM_m \quad \forall m \neq n \tag{23}$$

Two cells (C_n) and (C_m) are contiguous if there is a point P such that

$$PM_m = PM_n < PM_l \quad \forall l \neq m, n \tag{24}$$

Hence, the boundaries of the cells are bisecting planes in 3D and bisecting lines in 2D, and each cell contains only one point. This procedure can be applied in the case of monodisperse circular or spherical particles, and each cell will contain only one particle. In the case of contact between two particles, the bisecting plane is the tangent plane at the contact point; see Fig. 14.

2.5.2 Dirichlet cells

The Voronoi tessellation can still be used in the case of polydisperse spherical/circular particles (e.g. by considering the particle centers), but it leads to cells cutting through the particles. In order to assign one particle to each cell, the Dirichlet tessellation can be used. The boundary of a cell is defined by polygonal planes/lines which are radical planes/axes defined as the locus of points which have equal tangents to the two considered spheres/circles; see Fig. 14. When the two particles are in contact, the radical plane/line is the tangent plane/line at the contact point.

2.5.3 General case

For particles of arbitrary shape, a modified version of Voronoi tessellation may be employed. Let $d(P, G)$ be the distance from a point P to the particle (G).

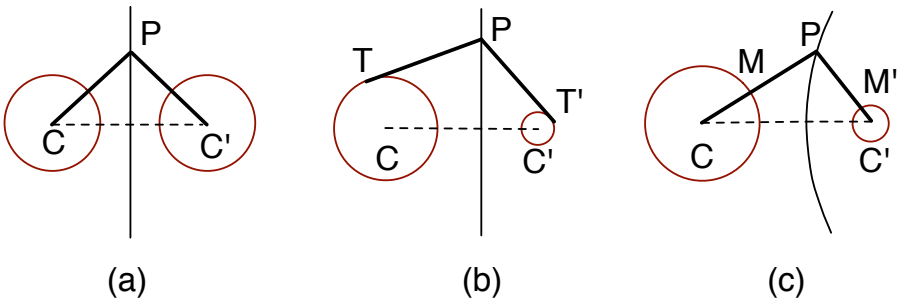

Fig. 14. Definition of the points P for three different tessellation rules: (a) Voronoi $PC = PC'$, (b) Dirichlet ($PT = PT'$), and (c) Modified Voronoi ($PM = PM'$).

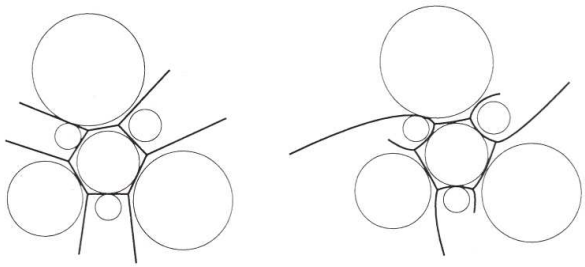

Fig. 15. Examples of tessellation for 7 circular particles: (a) Dirichlet cell, (b) modified Voronoi cell.

The cell (C_n) assigned to the particle (G_n) is defined by the set of points P such that

$$P \in (C_n) \quad \text{if} \quad d(P, G_n) < d(P, G_m) \quad \forall m \neq n \tag{25}$$

If this definition is applied to circular particles with different radii, it is easy to show that the boundaries of the cells are portions of hyperbola; see Fig. 15. For polygonal particles, the boundaries are lines and portions of parabola. For arbitrary particle shapes, the shape of the boundary depends on the particle shape. Note that the definition [**??**] does not require the choice of particular points inside the particles.

2.5.4 Neighborhoods and local void ratios

The tessellation of space is a powerful tool which allows for a continuum description of space in association with a discrete granular texture and provides a framework for the definition of local quantities associated with the particles and contact network. For example, the first neighbors of a particle (G_n) are easily identified with the particles (G_m) whose cells (C_m) are contiguous with the cell (C_n) associated with particle (G_n). In this way, to each side of the cell (C_n), a neighbor of particle (G_n) is associated. Let N_{vn} be the number of neighbors of particle (G_n) and N_p the total number of particles in the assem-

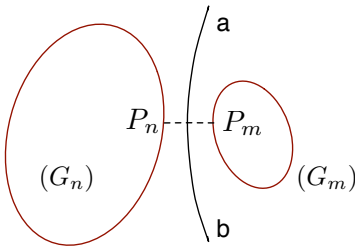

Fig. 16. Definition of potential contact for two particles (G_n) and (G_m); (ab) is the common face of the two corresponding cells and $g = P_nP_m$ is the gap.

bly. The mean number z_v of neighbours per particle in the assembly is given by

$$z_v = \frac{1}{2N_p} \sum_{n=1}^{N_p} N_{vn} \tag{26}$$

The definition of particle neighborhood can be used to define the notions of "potential contact" and "gap" (Fig. 16) which are important for numerical modeling of granular materials. Two particles (G_n) and (G_m) have a potential contact if they are neighbors, and their gap is $g = P_nP_m$ where P_n and P_m are the two proximal points on their boundaries. From a mechanical point of view, with the rigid body assumption, a contact is active only if the gap g vanishes and the contact can bear a normal force. The coordination number z is the mean number of active contacts per particle with $z \leq z_v$.

The space tessellationcan also be used to define local void ratios. When the particle deformations are neglected and no overlap occurs between the particles, each cell represents the free volume occupied by the particle contained in the cell. Let V_{vn} be the volume of the cell (C_n) and V_{sn} the volume of particle (G_n). The local void ratio is given by

$$e_{vn} = \frac{V_{vn}}{V_{sn}} \tag{27}$$

Given a space tessellation, a dual division of space called Delaunay triangulation, can be defined; Fig. 17. Let P_n be a point inside the particle (G_n). This point may be chosen arbitrarily but it is usually the geometrical or inertial center of the particle. The Delaunay triangulation is obtained by simply connecting the points belonging to neighboring cells. In this network, the material points P_n are the nodes and the elements are triangles in 2D and tetrahedra in 3D surrounding the intergranular voids. This duality can be used to define macroscopic quantities (Bagi [1996]). The cells (C_n) allow for the definition of neighbors and contacts. As a result, a stress tensor can be associated with each cell from the forces acting by the neighboring cells. On the other hand,

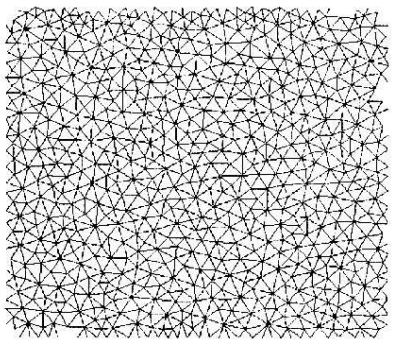

Fig. 17. Delaunay triangulation for the sample presented in Fig. **??**.

a strain tensor can be assigned to each Delaunay cell from the displacements of its nodes.

3 Granular kinematics

The plastic deformation of a granular system is fully characterized by the rigid-body translational and angular velocities of the particles. In the case of small strains from an initial to a deformed configuration, the displacement of the center of mass and rotation of each particle can be used. While the particles follow on average the motion imposed by external loading, strong deviations from the mean are observed. We discuss in this section both the average and fluctuating particle displacements and rotations. We also consider the issue of local strains and strain localization.

3.1 Particle displacements and rotations

Three examples of the displacement fields are displayed in Fig. 18 for biaxial compression, simple shear test and a combined strain path. In the same figure, the streamlines corresponding to a homogeneous deformation of the sample are plotted. These streamlines are deduced from the boundary conditions and assuming a homogeneous deformation. The general expression of the displacement field in the geometry of the $1\gamma 2\varepsilon$ setup is

$$u_x = ax + by \tag{28}$$
$$u_y = cy \tag{29}$$

where the constants a, b and c are determined from the deformation of the frame surrounding the granular sample. The streamlines are classically de-

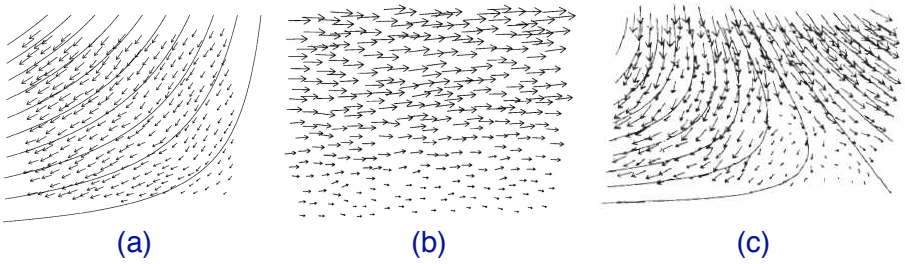

Fig. 18. Experimental displacement fields of particle centers for three different loadings: (a) biaxial compression, (b) simple shear and (c) biaxial compression followed by simple shear. The solid lines show streamlines deduced from the assumption of a homogeneous continuum deformation.

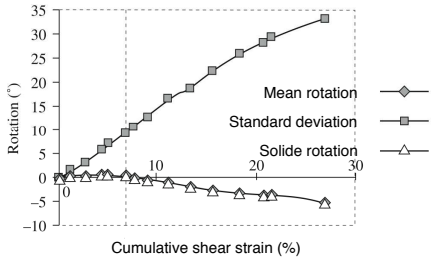

Fig. 19. Evolution of the mean $\langle\omega\rangle$ and standard deviation $\Delta\omega$ of particle rotations, as well as the solid rotation (anti-symmetric part of the displacement field), during a biaxial compression followed by simple shear.

duced by integrating

$$\frac{dx}{u_x} = \frac{dy}{u_y} \tag{30}$$

A good agreement is observed between the continuum mechanics prediction and measured displacements of rod centers. Nevertheless, the discrete nature of the material gives rise to fluctuations around these mean displacements (see below).

3.2 Rolling vs. sliding

Sliding and rolling occur at persistent contact points during deformation. At a purely rolling contact the friction force f_t is partially activated, i.e. $f_t \leq \mu f_n$, where f_n is the normal force and μ is the coefficient of friction. For two contacting particles (G_n) and (G_m) at a point C, the condition of rolling without sliding implies

$$\vec{V}_s(C) = \{\vec{V}(O_m) + \omega_m \times \vec{O}_m C\} - \{\vec{V}(O_n) + \omega_n \times \vec{O}_n C\} = 0 \tag{31}$$

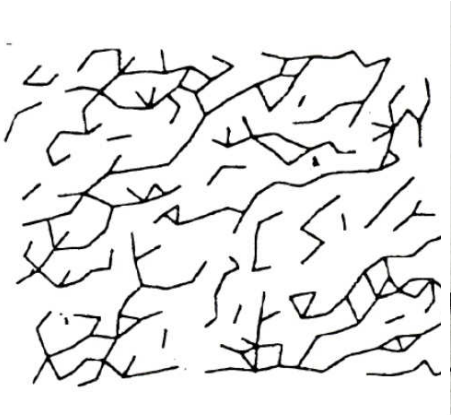

Fig. 20. The network of rolling contacts in a simple shear test by the $1\gamma 2\varepsilon$ setup.

where $V_s(C)$ represents the sliding velocity at the contact C, and O_m, O_n, ω_m and ω_n are the centers and spin vectors of (G_n) and (G_m).

The contact point C corresponds to the superposition of two material points attached to the two particles: $C_n \in (G_n)$ and $C_m \in (G_m)$. For the reference configuration, the contact point is $C_1 \equiv C_n \equiv C_m$. For a deformed configuration, the contact point C_1 is replaced by another point C_2, and the material points C_n and C_m at the boundaries of the two particles do not coincide any more. Let us consider the oriented arc lengths $a = C_2C_n$ and $b = C_2C_m$. The condition of rolling without sliding implies $a + b = 0$. This condition may be used to detect rolling contacts from particle displacements and rotations in experiments and numerical simulations (Lanier and Jean [2000], Oda et al. [1982], Dedecker et al. [2000]). One example is shown in Fig. 20 in the case of a shear test. We observe that most contacts are rolling (nearly 80%) and they tend to point in the principal stress direction (45° in shear test).

In numerical simulations, the rolling contacts can be determined from the condition $f_t < \mu f_n$, where f_n is the normal force, f_t is the tangential force and μ is the coefficient of friction. An example is displayed in Fig. 21 where the sliding contacts are marked in a sample of 4000 particles. Only, about 8% of contacts are in the sliding state. In the same figure, the weak and strong force networks are shown (see below). It is remarkable that all sliding contacts belong to the weak network, i.e. the contacts where the normal force is below the mean force.

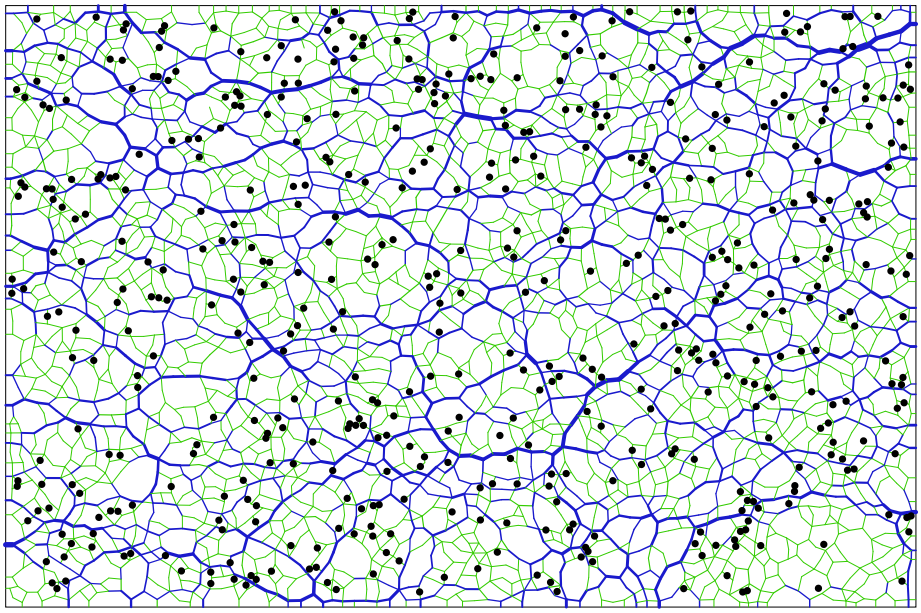

Fig. 21. The force-bearing network of contacts in a biaxially compressed system of 4000 disks. The line thickness is proportional to the normal force. The strong and weak forces are shown in dark and light colors, respectively. The sliding contacts are marked by small filled circles.

3.3 Fluctuating displacement fields

3.3.1 Uniform strain and fluctuations

We consider here the particle displacements in slow 2D granular flows. The displacements reflect the loss of stability of the particles, resulting in transition to new equilibrium states. Hence, the displacements are intimately correlated with force fluctuations in time (Bratberg et al. [2005], Taboada et al. [2005]). As in the case of force chains, the macroscopic homogeneity of shearing should be ensured in order to extract a meaningful statistics for intrinsic fluctuations. In simulations, this is achieved by means of periodic boundary conditions (Radjai and Roux [2002, 2004]). The displacement field, however, is not periodic if the mean strain is non-zero. In plane shear, it contains an affine part $\delta r^i \equiv (\delta r^i_x, \delta r^i_y)$, where i is the particle label, in addition to a periodic fluctuating field $\delta s^i \equiv (\delta s^i_x, \delta s^i_y)$ of zero mean ($\langle \delta s \rangle = 0$). The physical mechanism underlying the fluctuating field δs^i is the mismatch of the uniform strain field with mutual exclusions of the particles. As a result, the local strains deviate from the mean (far-field) strain.

In the simulations with bi-periodic boundary conditions, the particles can be driven by imposing the affine component $\delta {r_x}^i = \delta t \gamma r^i_y$, where γ is a constant shear rate and δt is the time step. In other words, the Fourier mode $k = 0$ of the total strain is imposed, corresponding to large scale forcing. Our focus

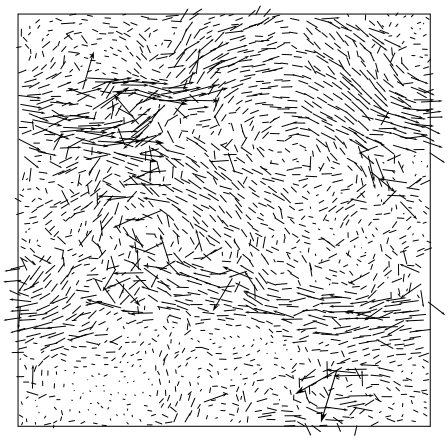

Fig. 22. A snapshot of particle displacements δs^i with respect to the mean background flow.

here is on the fluctuating components $(\delta s_x^i, \delta s_y^i)$ in the steady state where $\langle \delta {r_y}^i \rangle \simeq 0$.

Since we are interested in time scales beyond the elastic response time, the particle velocities should be evaluated from particle displacements. We consider the periodic part of the velocity field, and we define the fluctuating velocities v^i as a function of the integration time τ by

$$v^i(t, t+\tau) = \frac{1}{\tau} \int_t^{t+\tau} \delta s^i(t')\ dt' \tag{32}$$

In steady flow, the statistical properties of v are independent of t although they crucially depend on τ. Although dynamic simulations involve the physical time, the inertial effects are negligible and the contact network evolves quasistatically at time scales well below γ^{-1}. We normalize all times by γ^{-1} so that the dimensionless time t represents the cumulative shear strain. We also use the mean particle diameter d to scale displacements. As a result, the velocities will be scaled by γd and the power spectra in space by $(d^2\gamma)^2$.

Fig. 22 displays a snapshot of fluctuating velocities v^i for a short time lag $\tau = 10^{-5}$ in the simulations. We observe that large-scale well-organized displacements coexist with a strongly inhomogeneous distribution of amplitudes and directions on different scales. Convection rolls appear quite frequently, but they survive typically for strains τ less than 10^{-3}. After such short times, large-scale rolls break down and new statistically uncorrelated structures appear. This behaviour is thus radically different from turbulence eddies which survive long enough to undergo a significant distortion due to fluid motion.

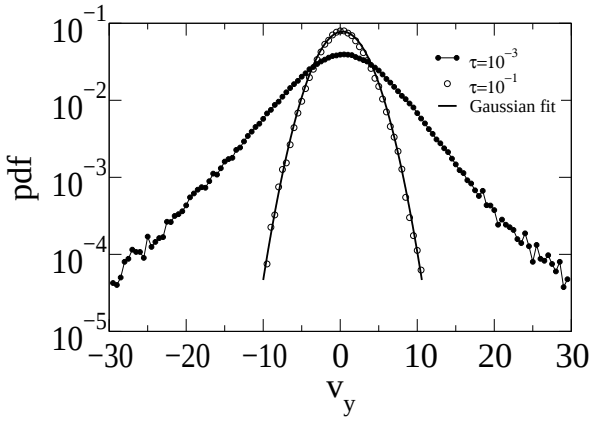

Fig. 23. Probability density functions of the y-components of fluctuating velocities for two different time resolutions: 10^{-3} (broad curve) and 10^{-1} (narrow curve). The latter is fitted by a Gaussian

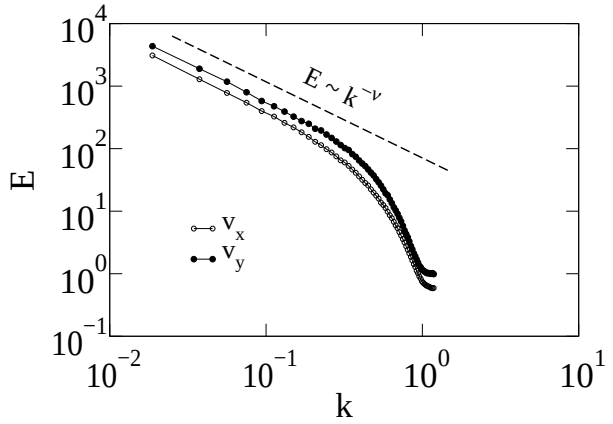

Fig. 24. Averaged power spectrum of the x and y components of the fluctuating velocity field with $\tau = 10^{-7}$ for one-dimensional cross sections along the mean flow.

3.3.2 Probability densities

An interesting issue is how the velocity distributions depend the on time resolution τ. In fluid turbulence, the phenomenon of intermittency, i.e. strong localized energy transfers at small scales, leads to the broadening of the exponential tails of the distributions of velocity differences at increasingly smaller scales. The distributions of v_y^i are shown in Fig.23 for a small integration time $\tau = 10^{-3}$, and for a large integration time $\tau = 10^{-1}$. We see that thedistribution has changed from a nearly Gaussian shape at large τ to a non-Gaussian shape with broad stretched exponential tails extending nearly to the center of the distribution at small τ. This non-Gaussian broadening of the distributions as a function of τ is observed also for the component v_x. The transition toward a Gaussian distribution for large time lags is a sign of partial loss of correlation and/or exhaustion of large fluctuations (Radjai and Roux [2002]).

3.3.3 Spatial correlations

The extent of spatial correlations may be estimated by considering the power spectrum E of fluctuating velocities along and perpendicular to the flow. The averaged spectrum on one-dimensional cross sections of the sheared packing is shown in Fig.24. The Fourier transform is performed over the fluctuating velocity field defined on a fine grid by interpolating the velocities from particle centers. The power spectra are quite similar along and perpendicular to the flow, and for different snapshots of the flow. They have a clear power-law shape $k^{-\nu}$ ranging from the smallest wavenumber $k = d/L$, corresponding to the system size L, up to a cut-off around $k = 0.5$, corresponding to nearly two particle diameters. The exponent is $\nu \simeq 1.24 \simeq 5/4$ over nearly one decade. This means that the fluctuating velocity field is self-affine.

The "intensity" of the velocity fluctuations, defined as the ratio of the root mean square displacement to the convective displacement of a particle, is about 2%. This amount of displacement is, however, sufficient to modify the kinematics in the vicinity of a particle, a local information that has a crucial consequence for our description of the fabric evolution and plastic volume change in granular media.

3.3.4 Granulence

The transition of velocity distributions from stretched exponential to gaussian as the time lag is increased and the power-law spectrum of the velocity field, as well as the superdiffusive character of particle motion (not shown here), bear a remarkable analogy with the scaling features of fluid turbulence (Radjai and Roux [2002]). Turbulence studies focus mainly on velocity differences δv measured at a fixed point of a fluid over a time interval τ or between two points separated by a distance r. This is in contrast with granular flow which involves a discrete displacement field that is carried by individual particles. Up to this difference in framework, the scaling properties discussed above are shared by turbulent fluid flows. The power-law scaling $k^{-\nu}$ for the spectrum of velocity differences is a hallmark of 3D turbulence with $\nu \simeq 5/3$ (to be compared with $\nu \simeq 5/4$ in our granular flow).

The observed analogy between granular velocity fluctuations and fluid turbulence in terms of scaling characteristics upgrades kinematic fluctuations in quasistatic granular flow to the rank of a systematic phenomenology which has been coined by the term "granulence" as compared to "turbulence" in fluid dynamics. Remark that this analogy works with three-dimensional turbulence although the simulation data concern a two-dimensional granular flow.

The fluctuating velocities and their scaling behavior are important for modeling the plastic behavior of granular materials from particle-scale considera-

tions. The self-affine nature of particle displacement fields means that uniform strain in a granular flow is accommodated via correlations at all scales. This behavior does not imply that velocity correlations extend to infinity under arbitrary boundary conditions. The observed scaling characteristics are a consequence of uniform shear. An interesting consequence is that uniform strain is easily disturbed as a result of the details of confining conditions or symmetry breaking agents such as a bulk force. In other words, disturbing the long-range correlations leads to nonuniform behavior. This might be the origin of the well-known property of granular materials to localize spontaneously the strain.

3.4 Local and global strains

In continuum mechanics, the local strain is defined by the displacement gradient at a given point of the material. The displacement field is assumed to be a continuous function of the coordinates. In granular media, the particles are not the volume elements of a continuum, and hence the local strain, i.e. the strain at the particle scale, is not simply given by the gradient of the particle displacement field. Only at larger scales, i.e. at the scale of a representative volume element of the material, the mean macroscopic strain in the sense of continuum mechanics can be defined. Here, we introduce a definition of local strains on the basis of particle neighborhood in the sense of adjacent cells of a tessellation. We then use this definition to study strain localization.

3.4.1 Particle-scale strain

Let us consider a particle (G) and its neighbors (G_i) with their centers O_i. Let (L) be the polygonal line which connects the points O_i and (S) the surface of this polygon; see Fig. 25. As the points O_i are material points, their displacements are well defined. The mean value of the displacement gradient is given by

$$\langle \partial_\beta u_\alpha \rangle = \frac{1}{S} \int\limits_{(S)} \partial_\beta u_\alpha dS = \frac{1}{S} \int\limits_{(L)} u_\alpha n_\beta \, d\ell \tag{33}$$

where $\vec{n}(n_\beta)$ is the unit normal vector of (L). To perform this integration, we should extrapolate the displacements to all points of space since u_β is known only at the points O_i. Assuming a linear approximation along each side of the polygon, we get

$$\langle \partial_\beta u_\alpha \rangle = \frac{1}{2S} \sum_{k=1}^{N_v} n_\beta^{(k)} (u_\alpha^{(k)} + u_\alpha^{(k+1)}) \ell^{(k)} \tag{34}$$

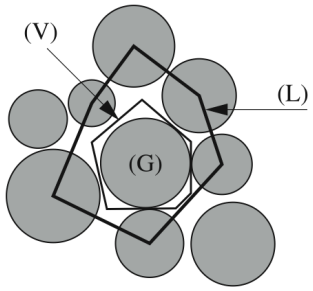

Fig. 25. Definition of local strain in the neighborhood of particle (G). The polygonal line (L) connects the centers of the neighboring particles according to the Dirichlet cell (V).

where $\ell^{(k)}$ is the length of the side labelled k, $n^{(k)}$ is the unit normal of this side, and $u^{(k)}$ and $u^{(k+1)}$ are the displacements of two successive corners. The strain tensor associated with particle (G) is then the symmetric part of $\langle \partial_\beta u_\alpha \rangle$.

It is worth noting that the expression [34] does not take into account the particle rotations. On the other hand, it concerns only the immediate neighborhood of each particle involving a volume of three particles which is far from a representative volume element. As a consequence, this local strain should rather be considered as a discrete measure of local deformation. Actually, the macroscopic strain is defined through a similar approach with a polygonal line (L) surrounding a representative volume element. The approximate linear size of such a volume is of the order of 15 to 20 particles (Calvetti et al. [1997]).

3.4.2 Strain localization

Strain localization is an important topic of research in soil mechanics. In classical laboratory tests such as triaxial compression and plane strain compression, the homogeneity of strain is necessary for the characterization of the material. But in practice, it is virtually impossible to avoid the localization of strain into shear bands. Incremental analysis of deformation by stereo-photogrammetry shows that the strain is more or less homogeneous at the beginning of compression, but as the stress state approaches the peak stress, the strain concentrates into shear bands (Desrues et al. [1983, 1996]). The thickness of the shear bands is generally estimated to vary from 10 to 20 particle diameters in the case of sand with narrow size distribution. It is also a general observation that strong dilatancy occurs inside the shear bands if the material is initially dense.

In 2D experiments by the $1\gamma 2\epsilon$ apparatus, the local shear intensities $E = \varepsilon_1 - \varepsilon_2$ can be evaluated from the local strains. Fig. 26 shows a map of local shear intensities, represented by squares of size proportional to E, in biaxial compression. We observe two main shear bands across the sample with reflections on the walls. The same system was simulated by means of the contact dynamics method (Lanier and Jean [2000]). As shown in Fig. 27, a similar shear-banding

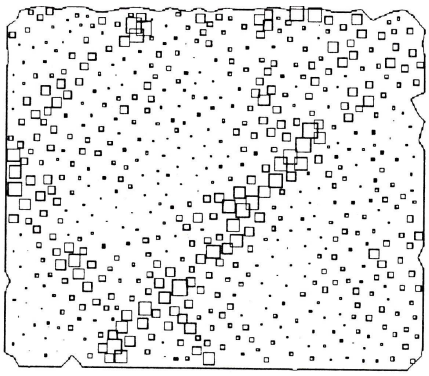

Fig. 26. Strain localization in a biaxial compression test by the $1\gamma 2\epsilon$ apparatus. The square size is proportional to the local shear intensity.

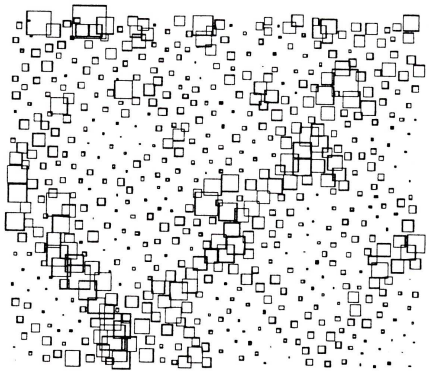

Fig. 27. Strain localization in a simulated biaxial compression with a sample whose initial configuration is the same as in the experiments (see Fig. 26). The square size is proportional to the local shear intensity.

pattern in position and thickness is obtained if the initial particle configuration in the simulations is the same as in the experiments. An initial configuration even slightly different from the experimental configuration does not lead to the same shear patterns. This sensitivity to the initial configuration makes the shear bands difficult to predict.

4 Conclusion

Many concepts and notions developed in this report are currently used for the description and modeling of granular media. For example, the fabric tensors are important for the characterization of the texture. Some other aspects, such as particle velocity fluctuations, are less well known but they provide the necessary information for a refined characterization of granular flows. As far as the relation between granular texture and quasi-static rheology is concerned, some hints were given. This is an active research area and one of the goals

of the present book. The approach followed in this chapter was based on the local vectors associated with a pair of contacting particles. The granular texture was then described in terms of the statistical distributions and spatial correlations of these vectors. However, in a statistical approach to the particle equilibrium states, which underly the yield properties of a granular medium, the fabric tensors are not sufficient. The description of the environment of a particle requires multi-contact probability density functions $g_c(\vec{n}_1, \ldots, \vec{n}_c)$ corresponding to the probability that the contact neighbours of a particle with c contact neighbors occupy the angular positions $\vec{n}_1, \ldots, \vec{n}_c$ around the particle (Roux and Radjai [2001], Troadec et al. [2002]). Both the connectivity function $P(c)$ and g_c are controlled by steric constraints of the particles, i.e. mutual exclusions together with excluded-volume effects, that impose an upper bound on the number of contact neighbors. In the same way, the flow behavior involves a statistical characterization of void cells. We did not introduce these aspects although interesting material can be found in the literature. Only basic definitions, such as different tessellation methods, were given as a first step towards a statistical description at the mesoscopic scale.

We did not consider the important issue of disorder and its nature in granular media. In particular, it is essential to distinguish between topological and metric disorders because of the unilateral character of contact between rigid particles. In granular media, the topological disorder, i.e. disorder related to particle connectivity, is more fundamental. Moreover, the description of metric disorder, i.e. the spatial correlations of particle positions, requires an extension of classical functions such as pair correlation functions in order to account for particle size polydispersity.

References

E. Azéma, G. Saussine, and F. Radjai. Quasistatic rheology, force transmission and fabric properties of a packing of irregular polyhedral particles. *Mechanics of Materials*, to appear., 2008.

Emilien Azma, Farhang Radja, Robert Peyroux, and Gilles Saussine. Force transmission in a packing of pentagonal particles. *Phys Rev E Stat Nonlin Soft Matter Phys*, 76(1 Pt 1):011301, Jul 2007.

K. Bagi. Stress and strain in granular assemblies. *Mechanics of Materials*, 22: 165–177, 1996.

I. Bratberg, F. Radjai, and A. Hansen. Intermittent flow of a collection of rigid frictional disks in a vertical pipe. *Phys. Rev. E*, 71(1 Pt 1):011301, Jan 2005. B.

F. Calvetti, G. Combe, and J. Lanier. Experimental micromechanical analysis of a 2d granular material: relation between structure evolution and loading path. *Mech. Coh. Frict. Materials*, 2:121–163, 1997.

B. Cambou. From global to local variables in granular materials. In C. Thornton, editor, *Powders and Grains 93*, pages 73–86, Amsterdam, 1993. A. A. Balkema.

F. Dedecker, M. Chaze, Ph. Dubujet, and B. Cambou. Specific features of strain in granular materials. *Mech. Coh. Frict. Materials*, 5:173–193, 2000.

. Desrues, J. Lanier, and P. Stutz. Localization of deformation in tests on sand samples. *Eng. Fracture Mechanics*, 21:p909–921, 1983.

J. Desrues, R. Chambon, M. Mokni, and F. Mazerolles. Void ratio evolution inside shear band in triaxial sand specimens studied by computed tomography. *Géotechnique*, 46:529–546, 1996.

K. I. Kanatani. Distribution of directional data and fabric tensors. *Int. J. Ingng. Sci*, 22:149–164, 1984.

J. Lanier and M. Jean. Experiments and numerical simulations with 2d disks assembly. *Powder Technology*, 109:206–221, 2000.

M. Oda and K. Iwashita, editors. *Mechanics of Granular Materials*. A. A. Balkema, Rotterdam, 1999.

M. Oda, J. Koshini, and S. Nemat-Nasser. Some experimentally based fundamental results on the mechanical behavior of granular materials. *Geotechnique*, 30:479–495, 1980.

M. Oda, J. Konishi, and S. Nemat-Nasser. Experimental micromechanical evaluation of strength of granular materials: effects of particle rolling. *Mechanics of Materials*, 1:269–283, 1982.

H. Ouadfel and L. Rothenburg. Stress-force-fabric relationship for assemblies of ellipsoids. *Mechanics of Materials*, 33(4):201–221, 2001.

F. Radjai and S. Roux. Contact dynamics study of 2d granular media : Critical states and relevant internal variables. In H. Hinrichsen and D. E. Wolf, editors, *The Physics of Granular Media*, pages 165–186, Weinheim, 2004. Wiley-VCH.

F. Radjai, H. Troadec, and S. Roux. Key features of granular plasticity. In S.J. Antony, W. Hoyle, and Y. Ding, editors, *Granular Materials: Fundamentals and Applications*, pages 157–184, Cambridge, 2004. RS.C.

Farhang Radjai and Stphane Roux. Turbulentlike fluctuations in quasistatic flow of granular media. *Phys Rev Lett*, 89(6):064302, Aug 2002.

L. Rothenburg and R. J. Bathurst. Analytical study of induced anisotropy in idealized granular materials. *Geotechnique*, 39:601–614, 1989.

S. Roux and F. Radjai. Statistical approach to the mechanical behavior of granular media. In H. Aref and J.W. Philips, editors, *Mechanics for a New Millennium*, pages 181–196, Netherlands, 2001. Kluwer Acad. Pub.

M. Satake. Fabric tensor in granular materials. In P. A. Vermeer and H. J. Luger, editors, *Proceedings of the IUTAM symposium on deformation and failure of granular materials, Delft*, pages 63–68, Amsterdam, 1982. A. A. Balkema.

A. Taboada, K. J. Chang, F. Radjai, and F. Bouchette. Rheology, force transmission, and shear instabilities in frictional granular media from biaxial numerical test using the contact dynamics method. *Journal Of Geophysical*

Research, 110:1–24, 2005.

H. Troadec, F. Radjai, S. Roux, and J.C. Charmet. Model for granular texture with steric exclusion. *Physical Review E*, 66(4 1):041305–1, 2002. ISSN 1063-651X.

Charles Voivret. *Texture et comportement des matériaux granulaires à grande polydispersité*. PhD thesis, Université Montpellier 2, 2008.